Materials Research Proceedings 37 (2023) 679-689 https://doi.org/10.21741/9781644902813-146

Numerical suite for the design, simulation and optimization of cathode-less plasma thrusters

Nabil Souhair[1,2,a *], Mirko Magarotto[3,b], Raoul Andriulli[1,c], Fabrizio Ponti[1,d],

[1] Alma Propulsion Laboratory, Department of Industrial Engineering, University of Bologna, Forlì, 47122, Italy

[2] LERMA Laboratory, Aerospace and Automotive Engineering School, International University of Rabat , Sala al Jadida, Rabat, 11100, Morocco

[3] Department of Electric Engineering, University of Padova, Padova, 35131, Italy

[a]nabil.souhair2@unibo.it, [b]mirko.magarotto@unipd.it, [c]raoul.andriulli@unibo.it, [d]fabrizio.ponti@unibo.it

Keywords: Space Propulsion, Electric Propulsion, Cathode-Less Plasma Thrusters, Plasma Thrusters, Numerical Simulations, Global Plasma Models, Multi Fluid Approach, Particle-In-Cell

Abstract. A numerical suite developed for the analysis and design of cathodeless plasma thrusters is presented. The suite includes a Global Model that estimates the thruster's propulsive performance by means of a balance of electron energy and population density, and a 3D numerical strategy to assess plasma behavior. The suite incorporates a FLUID and EM modules to solve plasma transport and electromagnetic wave propagation within the discharge chamber. The PLUME module, managed by the Starfish code, handles plasma dynamics in the magnetic nozzle using the electrostatic particle-in-cell approach. The suite has been validated against thrust measurements from a Helicon Plasma Thruster demonstrating the suite's potential for optimizing the design and operation of cathodeless plasma thrusters for space propulsion applications.

I Introduction

In the last decade, an active research has been conducted on the electric propulsion field [1,2]. Particular effort has been put in the development of cathodeless systems such as Helicon Plasma Thrusters (HPT) [3,4] and Electron Cyclotron Resonance Thrusters (ECRT) [5]. In these devices, plasma is produced within a dielectric tube where the neutral gas propellant is injected. An antenna, operated in the Radio Frequency (RF) or in the microwave frequency range, sustains the discharge coupling Electromagnetic (EM) power to the plasma [6]. Magnets produce a magnetostatic field that has three main functions: (i) increasing the efficiency of the source by enhancing the plasma confinement [7], (ii) driving the power coupling between the antenna and the plasma [8], (iii) improving the propulsive performance via the magnetic nozzle effect downstream the thruster outlet [9-12].

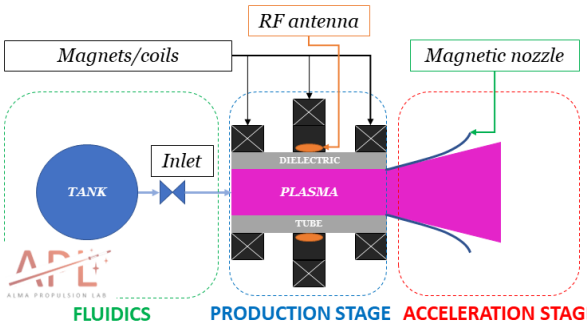

Figure 1. Schematic of a cathodeless plasma thruster. Magnetic field lines highlighted within the plasma source.

The key physical phenomena that govern the plasma dynamics in the production stage, with reference to Figure 1, are the EM wave propagation [13], the plasma transport [14], and their mutual coupling [15]. Instead, the acceleration and detachment phenomena [16] take place

Materials Research Proceedings 37 (2023) 679-689 https://doi.org/10.21741/9781644902813-146

downstream the plasma source in the region identified as acceleration stage (see Figure 1). The latter is characterized by the formation of a plume where the plasma is more rarefied (density in the range 10^{16} - 10^{18} m^{-3}) than in the production stage [17]. Particle collisions and the geometry of the applied magnetostatic field govern the plasma behaviour in the region closer to the thruster [18]. Further downstream, the plasma expansion is driven by the thermal pressure, and the ambipolar diffusion [18]. Several analytical [19-21] and numerical approaches have been pursued in the literature for modelling both the production stage and the acceleration stage. The most relevant are: fluid [22], kinetic [23], Particle In Cell with Monte Carlo collisions (PIC-MCCs) [24], and hybrid [25].

In this work, a numerical suite for cathodeless plasma thrusters is presented and its exploitation in a low power case is discussed. A Global Model is devoted to the preliminary estimation of the propulsive performance [26]. More advanced tools have been developed to predict the plasma dynamics throughout the thruster. The 3D-VIRTUS code solves, with a fluid approach, the plasma transport within the production stage. The PIC tools Starfish [27] and have been customized to simulate the plasma dynamics within the magnetic nozzle. Starfish, which handles 2D axisymmetric domains, has been coupled to 3D-VIRTUS in order to estimate the propulsive performance.

II Methodology

II.A Global Model

The main assumptions associated to the Global Model [26] are: (i) cylindrical geometry of the plasma source, (ii) axisymmetric magnetostatic field, (iii) the presence of cusps in the source can be simulated, (iv) the paraxial approximation holds in the acceleration stage [19], (v) in the acceleration stage plasma is frozen to the field lines up to the detachment. The dynamics of the source is solved relying on the conservation of mass (Eq.1) and electron energy (Eq.2) equations

$$\frac{dn_I}{dt} = R^I{}_{chem} - R^I{}_{wall} - R^I{}_{ex} + R^I{}_{in} \tag{1}$$

$$\frac{d}{dt}\left(\frac{3}{2}n_e T_e\right) = Pw - P_{chem} - P_{wall} - P_{ex} \tag{2}$$

n_I is the number density of the I-th species, being this study focused on a xenon plasma I=e, i, *, g for electrons, ions (Xe^+), excited (Xe^*), and ground state (Xe) particles respectively. T_e is the electron temperature in eV. R^I_{chem}, R^I_{wall}, R^I_{ex}, R^I_{in}, are the I-th particle source/sink terms associated to plasma reactions, wall losses, particles outflow and inflow respectively. Pw, P_{chem}, P_{wall}, P_{ex} are the power coupled to the plasma, along with the source/sink terms associated to plasma reactions, wall losses, and particles outflow respectively. The plasma reactions considered are elastic scattering, ionization and excitation (see Table 1), therefore the R^I_{chem} and P_{chem} terms read [29]

$$R^I{}_{chem} = \sum_J K_{JI} n_J n_e - \sum_J K_{IJ} n_I n_e \tag{3}$$

$$P_{chem} = \sum_I \sum_J K_{IJ} n_I n_e \, \Delta U_{IJ} + \sum_I K_{II} n_I n_e \frac{3m_e}{m_I} T_e \tag{4}$$

Where K_{IJ} is the rate constant for the inelastic transitions from species I to species J, K_{II} is the rate constant for elastic collisions between species I and electrons, ΔU_{IJ} is the energy difference (in eV) between species I and species J, along with m_e and m_I are the electron mass and I species

Materials Research Proceedings 37 (2023) 679-689 https://doi.org/10.21741/9781644902813-146

mass respectively [30]. Assuming the Bohm sheath criterion at the source walls [26] and a sonic thruster outlet, similar expressions hold for R^I_{wall} and R^I_{ex}

$$R^I{}_{wall} = \frac{S^I{}_{wall}}{V} \Gamma^I{}_{wall} \tag{5a}$$

$$R^I{}_{ex} = \frac{S^I{}_{ex}}{V} \Gamma^I{}_{ex} \tag{5b}$$

Where V is the volume of the source, S^I is the equivalent surface of the source, and Γ^I is the particles flux. For ions and electrons $S^e = S^i$ and its expression, which accounts for the non-uniformity of the plasma within the source, can be found in [30]. Similarly $\Gamma^e = \Gamma^i = n_e u_B$ where u_B is the Bohm speed [31]. For neutrals $R^g_{wall} =$ $-R^e_{wall}$ assuming total recombination at the walls [26]. Instead S^g_{ex} is equal to the physical thruster outlet surface and, assuming the neutrals are in the molecular regime, $\Gamma^g = 1/4\ n_g\ u_{th}$ [26]; u_{th} is the neutrals thermal speed [31]. From the Bohm sheath criterion, the energy terms read [26]

$$P_{wall} = R^e{}_{wall} \left(2 + \log \sqrt{\frac{m_i}{2\pi m_e}} \right) T_e \tag{6a}$$

$$P_{ex} = R^e{}_{ex} \left(2 + \log \sqrt{\frac{m_i}{2\pi m_e}} \right) T_e \tag{6b}$$

Regarding the gas inflow, only neutral species are assumed to be injected into the source

$$R^g{}_{in} = \frac{\dot{m}_0}{V m_g} \tag{7}$$

where $\dot{m}_0$ is the mass flow rate.

Table 1: plasma reactions considered.

Reaction	Formula	Reference
Elastic scattering	$e + Xe \rightarrow e + Xe$	[29]
Ionization	$e + Xe \rightarrow 2e + Xe^+$	[29]
Excitation	$e + Xe \rightarrow e + Xe^* \rightarrow e + Xe + h\nu$	[29]

The thrust is computed according to the model presented in [19]. The contribution from the plasma is

$$F_p = \frac{M_{det}{}^2 + 1}{M_{det}} q n_e T_e S^e{}_{ex} \tag{8}$$

where q is the elementary charge, and M_{det} is the magnetic Mach number (v/u_B) at the detachment point. M_{det} is computed according to the detachment criterion prescribed in [19]. The contribution to the thrust due to neutral gas expansion is

Materials Research Proceedings 37 (2023) 679-689 https://doi.org/10.21741/9781644902813-146

$$F_g = p_g S^g{}_{ex} \tag{9}$$

where p_g is the neutral pressure. Total thrust and specific impulse, being g_0 the standard gravity, read

$$F = F_p + F_g \tag{10a}$$

$$I_{sp} = \frac{F}{g_0 \dot{m}_0} \tag{10b}$$

II.B Source Solver

The plasma source is handled with the 3D-VIRTUS code [15]. Plasma transport and EM wave propagation are solved self-consistently by means of two distinct modules, namely the Fluid module and the EM module, run iteratively. In the former, the plasma transport is solved in a 2D domain while the latter relies on a 3D domain [13]. The governing equations of the fluid module are continuity, energy and Poisson

$$\frac{\partial n_I}{\partial t} + \nabla \cdot \boldsymbol{\Gamma}_I = R^I{}_{chem} \tag{11a}$$

$$\frac{\partial n_\varepsilon}{\partial t} + \nabla \cdot \boldsymbol{\Gamma}_\varepsilon - \nabla\varphi \cdot \boldsymbol{\Gamma}_e = Pw - P_{chem} \tag{11b}$$

$$\nabla^2 \varphi = -\mathrm{q}\left(\frac{n_i - n_e}{\varepsilon_0}\right) \tag{11c}$$

The species considered are electrons, ions (Xe^+) and neutrals (Xe). Where $n_\varepsilon = 3/2\ n_e\ T_e$ is the energy density, φ is the plasma potential and ε_0 is the permittivity of vacuum. Formally, the terms $R^I{}_{chem}$ and P_{chem} are reported in Eq.3 and Eq.4, but in 3D-VIRTUS they are scalar fields which depend on the position. Reactions considered are listed in Table 1. $\boldsymbol{\Gamma}_I$ is the particle flux of the species I that, according to the drift diffusion approximation, reads

$$\boldsymbol{\Gamma}_I = \pm \bar{\bar{\mu}}_I n_I \nabla\varphi - \bar{\bar{D}}_I \nabla n_I + \boldsymbol{u}_0 n_I \tag{12}$$

Where μ_I and D_I are the mobility and the diffusion coefficients of the species I whose values are prescribed in [32]. $\boldsymbol{u}_0$ is the convection speed assumed aligned with the thruster axis and equal, in modulus, to $1/4\ v_{th}$ [7]. $\boldsymbol{\Gamma}_\varepsilon$ is the energy flux that reads

$$\boldsymbol{\Gamma}_\varepsilon = \bar{\bar{\mu}}_\varepsilon n_\varepsilon \nabla\varphi - \bar{\bar{D}}_\varepsilon \nabla n_\varepsilon + \boldsymbol{u}_0 n_\varepsilon \tag{13}$$

Where μ_ε and D_ε are derived according to the Einstein relations [15]. The power deposition profile is computed via the EM module and it reads [15]

$$Pw = \frac{1}{2q} Re(\boldsymbol{J}_{RF}{}^* \cdot \boldsymbol{E}_{RF}) \tag{14}$$

Where $\boldsymbol{J}_{RF}$ and $\boldsymbol{E}_{RF}$ are the complex values of the current density and electric field induced by the RF antenna onto the plasma.

A Robin type boundary condition is imposed to the electrons continuity and energy to enforce the Bohm sheath criterion [15]. A zero gradient Neumann type condition is imposed to the continuity of ions. At the walls, a Neumann condition is imposed to the continuity of the neutrals

Materials Research Proceedings 37 (2023) 679-689 https://doi.org/10.21741/9781644902813-146

in order to enforce the recombination of the charged species [15]. At the thruster outlet, the neutral density gradient is assumed null [7]. Finally, a Neumann type boundary condition is imposed to Poisson's equation to enforce the equality between ions and electrons fluxes at the walls [26]. The thruster outlet is grounded [15].

II.C Plume Solver

The plasma in the plume has been simulated with a fully kinetic Particle In Cell (PIC) solver, namely Starfish [27-28]. This handles axisymmetric domains even though the particles' speed is solved in 3D. Starfish has been coupled to 3D-VIRTUS in order to solve the plasma dynamics in the overall thruster and, in turn, to estimate the propulsive performance. The plasma in the acceleration stage is assumed collisionless [33], nonetheless the dynamics of both neutral (Xe) and charged species, namely electrons and ions (Xe^+), are tracked. Particles' speed is solved from the discrete equation of motion

$$\frac{\boldsymbol{v}^{t+\frac{1}{2}} - \boldsymbol{v}^{t-\frac{1}{2}}}{\Delta t} = \frac{q_I}{m_I}\left(\boldsymbol{E}^t + \frac{\boldsymbol{v}^{t+\frac{1}{2}} + \boldsymbol{v}^{t-\frac{1}{2}}}{2} \times \boldsymbol{B}^t\right) \tag{15a}$$

$$\frac{\boldsymbol{r}^{t+1} - \boldsymbol{r}^t}{\Delta t} = \boldsymbol{v}^{t+\frac{1}{2}} \tag{15b}$$

Where $\boldsymbol{r}^t$ is the particle position at time step t, $\boldsymbol{v}$ is the particle speed, Δt is the time step, $\boldsymbol{E}$ is the electric field and $\boldsymbol{B}$ the magnetic field. A Boris scheme is used to advance particles [34]. Since the RF power deposition in the acceleration stage is assumed negligible [35] the EM fields in the plasma are calculated via the Poisson's equation. Therefore, $\boldsymbol{B}$ consists in the background magnetostatic field and $\boldsymbol{E}=-\nabla\varphi$ where

$$\varepsilon_0 \nabla^2 \varphi = -\rho \tag{16}$$

and ρ is the charge density computed from particles position via a linear deposition scheme [33].

Regarding boundary conditions, Eq.17 holds for the Poisson's equation

$$\varphi = 0 \quad \text{Thruster outlet} \tag{17a}$$

$$\varphi = \varphi_\infty \quad \text{Thruster case} \tag{17b}$$

$$\frac{d\varphi}{dk} + \frac{1}{r}(\varphi - \varphi_\infty) = 0 \quad \text{External boundary} \tag{17c}$$

Where k is the direction normal to the external boundary, r is the distance between the centre of the thruster and the boundary, along with φ_∞ is the potential at infinity. Eq.17c derives from the assumption that $\varphi \approx 1/r$ for $r \to \infty$ [36]. Regarding particles dynamics, ions and electrons that reach the thruster outlet and the thruster case are removed from the simulation domain [35]. The same condition holds for the ions at the external boundary [35] where an energy-based condition is defined to account for the electrons "trapped" by the potential drop across the plume [37]. The total energy of each electron that reaches the external boundary is computed according to Eq.18

$$E_{tot} = \frac{1}{2} m_I v^2 - q_I \varphi \tag{18}$$

Materials Research Proceedings 37 (2023) 679-689 https://doi.org/10.21741/9781644902813-146

If $|E_{tot}|>|q\varphi_\infty|$ the electron is absorbed since its energy is high enough to escape at the infinity. If $|E_{tot}|\leq|q\varphi_\infty|$ the particle is considered "trapped" and it is subject to a specular reflection.
A control loop has been implemented in order to enforce the current free and the quasi-neutrality conditions at the thruster outlet. The value of the potential at infinity is updated according to Eq.19.

$$\varphi_\infty{}^{t+1} = \varphi_\infty{}^{t} + \frac{1}{C}\left(I_{iB}{}^{t} + I_{eB}{}^{t}\right)\Delta t \tag{19}$$

Where C is an equivalent capacitance used to tune φ_∞ so that the current free condition holds. The ion flux at the thruster outlet is assumed constant (Eq.20a) [35] instead the electron flux is varied according to Eq.20b to ensure quasi-neutrality

$$I_{i0} = \frac{q_i \dot{m}_0}{M} \tag{20a}$$

$$I_{e*}{}^{t+1} = K\frac{n_{i0}{}^{t}}{n_{e0}{}^{t}}\, I_{e*}{}^{t} \tag{20b}$$

K is a positive constant and I_{e*} is the emitted electron flux. It is worth noting that the total electron flux (I_{e0}) depends also on the number of electrons absorbed at the
thruster outlet which is mainly driven by the value of φ_∞ [35]. As a consequence the control strategy implemented relates φ_∞ to the flux of particles injected into the domain and allows to compute self-consistently the total potential drop across the plume (namely $-\varphi_\infty$).
Finally, the thrust is computed according the Eq.21 [25]

$$F = \int \sum_I \left(m_I n_I v_{Iz} \boldsymbol{v}_z \cdot \hat{\boldsymbol{k}} + p_I \hat{\boldsymbol{z}} \cdot \hat{\boldsymbol{k}}\right) dS_B \tag{21}$$

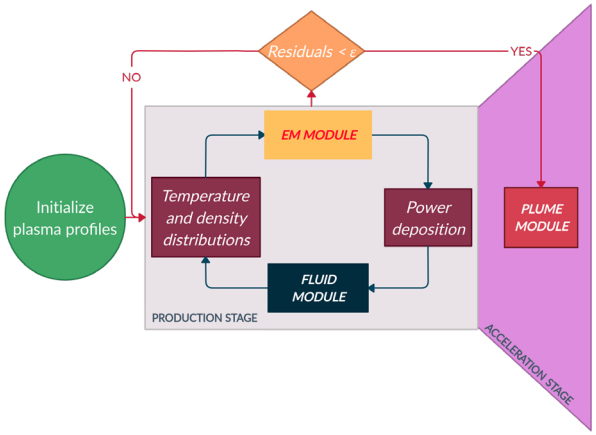

Figure 2. Schematic of the 2D thruster simulation tool. The Source solver (3D-VIRTUS) and the Plume solver (Starfish) run sequentially.

The coupling strategy between the production stage (i.e., 3D-VIRTUS) and the acceleration stage (i.e., Starfish) is schematically depicted in Figure 2. First, the source solver provides plasma profiles at the thruster outlet assuming a sonic condition for this boundary. Second the plume solver takes these profiles as an input and propagates the solution of the plasma expansion.

Materials Research Proceedings 37 (2023) 679-689 https://doi.org/10.21741/9781644902813-146

III Results

The thruster analysed in this work is a low power (50 W range) HPT. The plasma source is a cylinder whose dimensions are length L=0.060 m and diameter D=0.014 m. Magnetic field is generated by two rings of permanent magnets. At thruster outlet, the intensity of the magnetic field on the axis is B_0=600 G. The antenna is a five turns coil whose dimensions are length L_A=0.020 m, diameter D_A=0.020 m, wire width w_A=0.002 m. A mass flow rate of $\dot{m}_0$=0.15 mg/s has been assumed. The power provided to the antenna (Pw) varies in the range from 10 W up to 70 W. An antenna efficiency of η_A=0.8 has been assumed, so the power actually coupled to the plasma is $Pw_p = \eta_A\, Pw$.

A 2D simulation of the overall plasma thruster has been accomplished for an input power Pw=55 W. In Figure 3, the input power deposition profile adopted is shown, and is consistent with an inductive coupling mode [39,40].

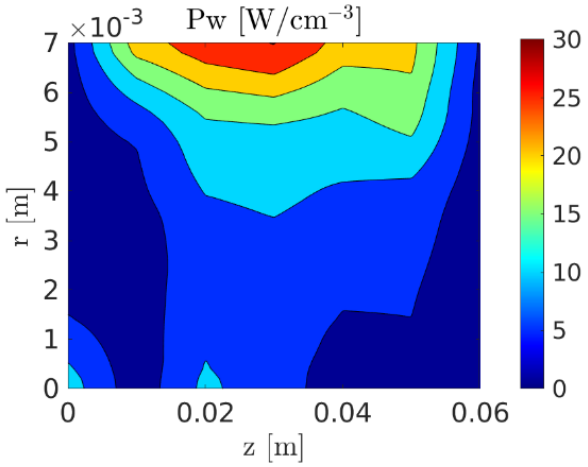

Figure 3. Deposited power map (Pw) function of the radial and axial positions (r-z) in the source.

The estimation of the propulsive performance obtained with both the GM and the 2D simulation of the HPT has been reported in Figure 4.

For what concerns the GM, due to the several assumptions considered, an uncertainty band of ±20% has been attributed to numerical results. The latter is mainly associated to the assumptions on plasma profiles (Eq.5) [26], interactions between the plasma and the walls of the source (Eq.6) [26], cross sections of the plasma reactions (Table 1) [26], and detachment criterion (Eq.8) [7]. The propulsive performance increases with the power coupled to the plasma. Trends predicted numerically and evaluated experimentally are in agreement. Moreover, numerical and experimental uncertainty bands overlap. This result can be considered sufficiently accurate for the scope of the GM which is meant for the preliminary characterization.

Regarding the 2D simulation, thrust has been computed coupling the solution of the production stage with both the semi-analytical formulation implemented in the Global Model (i.e., Eqs.8-10) and the results provided by Starfish (i.e., Eq.21). In both cases, the estimation of the propulsive performance matches better the experimental benchmark with respect to the Global Model. The most accurate result is provided coupling 3D-VIRTUS and Starfish being the difference between numerical and experimental results less than 20%.

Materials Research Proceedings 37 (2023) 679-689 https://doi.org/10.21741/9781644902813-146

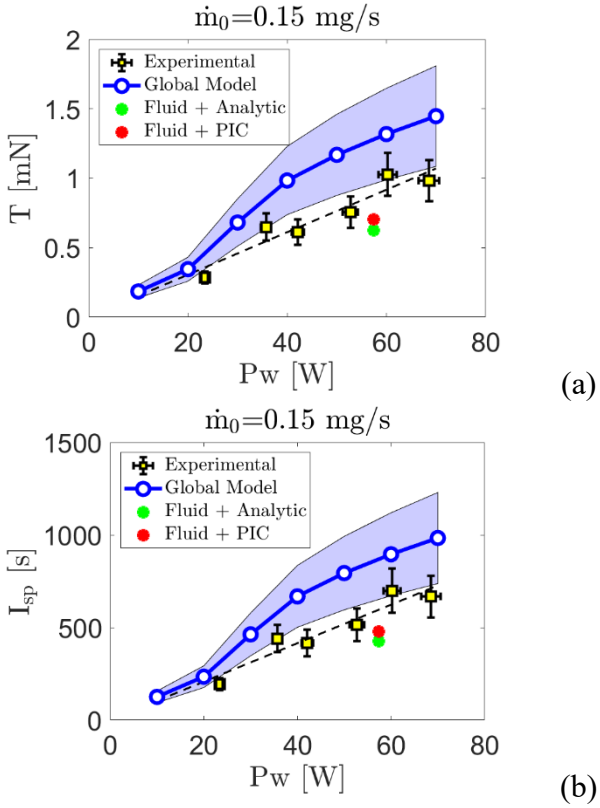

Figure 4. Performance predicted numerically compared against measures. (a) Thrust (T), and (b) specific impulse (I_{sp}) in function of the coupled power (Pw).

VI Conclusions

A numerical suite capable of simulating the propulsive performance and the plasma dynamics in a cathodeless plasma thruster is shown. It consists on a Global Model [26] for the preliminary simulation of the propulsive performance, the 3D-VIRTUS code [15] for the estimation of the plasma profile in the production stage, along with Starfish [27] for the solution of the acceleration stage. The results of the Global Model and of the coupling 3D-VIRTUS / Starfish have been benchmarked against measurements of the propulsive performance (i.e., thrust and specific impulse). The agreement between experiments and the Global Model is always better than 50%, whereas differences reduce to 20% with a multi-dimensional approach.

In future works the interfacing strategy between 3D-VIRTUS and Starfish will be improved adopting an iterative approach.

Finally, it is worth noting that the numerical suite presented in this work can simulate the plasma dynamics also in applications different from the electric propulsion as plasma antennas [43-47] and water treatment reactors [48].

References

[1] S. Mazouffre (2016). Electric propulsion for satellites and spacecraft: established technologies and novel approaches. Plasma Sources Science and Technology, 25(3), 033002. https://doi.org/10.1088/0963-0252/25/3/033002

[2] D. M. Goebel, I. Katz (2008). Fundamentals of electric propulsion: ion and Hall thrusters (Vol. 1). John Wiley & Sons. https://doi.org/10.1002/9780470436448

[3] K. Takahashi (2019). Helicon-type radiofrequency plasma thrusters and magnetic plasma nozzles. Reviews of Modern Plasma Physics, 3(1), 1-61. https://doi.org/10.1007/s41614-019-0024-2

[4] M. Manente, et al. (2019). REGULUS: A propulsion platform to boost small satellite missions. Acta Astronautica, 157, 241-249. https://doi.org/10.1016/j.actaastro.2018.12.022

[5] F. Cannat, T. Lafleur, J. Jarrige, P. Chabert, P. Q. Elias, D. Packan (2015). Optimization of a coaxial electron cyclotron resonance plasma thruster with an analytical model. Physics of Plasmas, 22(5), 053503. https://doi.org/10.1063/1.4920966

[6] D. Arnush, F. F. Chen (1998). Generalized theory of helicon waves. II. Excitation and absorption. Physics of Plasmas, 5(5), 1239-1254. https://doi.org/10.1063/1.872782

[7] M. Magarotto, M. Manente, F. Trezzolani, D. Pavarin (2020). Numerical model of a helicon plasma thruster. IEEE Transactions on Plasma Science, 48(4), 835-844. https://doi.org/10.1109/TPS.2020.2982541

[8] M. Magarotto, D. Melazzi, D. Pavarin (2019). Study on the influence of the magnetic field geometry on the power deposition in a helicon plasma source. Journal of Plasma Physics, 85(4). https://doi.org/10.1017/S0022377819000473

[9] E. Ahedo, M. Merino (2010). Two-dimensional supersonic plasma acceleration in a magnetic nozzle. Physics of Plasmas, 17(7), 073501. https://doi.org/10.1063/1.3442736

[10] N. Bellomo, et al. (2021). Design and In-orbit Demonstration of REGULUS, an Iodine electric propulsion system. CEAS Space Journal. https://doi.org/10.1007/s12567-021-00374-4

[11] A. V. Arefiev, B. N. Breizman (2004). Theoretical components of the VASIMR plasma propulsion concept. Physics of Plasmas, 11(5), 2942-2949. https://doi.org/10.1063/1.1666328

[12] K. Takahashi (2021). Magnetic nozzle radiofrequency plasma thruster approaching twenty percent thruster efficiency. Scientific reports, 11(1). https://doi.org/10.1038/s41598-021-82471-2

[13] D. Melazzi, V. Lancellotti (2014). ADAMANT: A surface and volume integral-equation solver for the analysis and design of helicon plasma sources. Computer Physics Communications, 185(7), 1914-1925. https://doi.org/10.1016/j.cpc.2014.03.019

[14] J. Zhou, D. Pérez-Grande, P. Fajardo, E. Ahedo (2019). Numerical treatment of a magnetized electron fluid model within an electromagnetic plasma thruster simulation code. Plasma Sources Science and Technology, 28(11), 115004. https://doi.org/10.1088/1361-6595/ab4bd3

[15] M. Magarotto, D. Melazzi, D. Pavarin (2020). 3D-VIRTUS: Equilibrium condition solver of radio-frequency magnetized plasma discharges for space applications. Computer Physics Communications, 247, 106953. https://doi.org/10.1016/j.cpc.2019.106953

[16] A. V. Arefiev, B. N. Breizman (2005). Magnetohydrodynamic scenario of plasma detachment in a magnetic nozzle. Physics of Plasmas, 12(4), 043504. https://doi.org/10.1063/1.1875632

[17] G. Sánchez-Arriaga, J. Zhou, E. Ahedo, M. Martínez-Sánchez, J. J. Ramos (2018). Kinetic features and non-stationary electron trapping in paraxial magnetic nozzles. Plasma Sources Science and Technology, 27(3), 035002. https://doi.org/10.1088/1361-6595/aaad7f

[18] F. Cichocki, A. Domínguez-Vázquez, M. Merino, E. Ahedo (2017). Hybrid 3D model for the interaction of plasma thruster plumes with nearby objects. Plasma Sources Science and Technology, 26(12), 125008. https://doi.org/10.1088/1361-6595/aa986e

[19] T. Lafleur (2014). Helicon plasma thruster discharge model. Physics of Plasmas, 21(4), 043507. https://doi.org/10.1063/1.4871727

[20] E. Ahedo, & J. Navarro-Cavallé (2013). Helicon thruster plasma modeling: Two-dimensional fluid-dynamics and propulsive performances. Physics of Plasmas, 20(4), 043512. https://doi.org/10.1063/1.4798409

[21] A. Fruchtman, K. Takahashi, C. Charles, R. W. Boswell (2012). A magnetic nozzle calculation of the force on a plasma. Physics of Plasmas, 19(3), 033507. https://doi.org/10.1063/1.3691650

[22] M. Magarotto, D. Pavarin (2020). Parametric study of a cathode-less radio frequency thruster. IEEE Transactions on Plasma Science, 48(8), 2723-2735. https://doi.org/10.1109/TPS.2020.3006257

[23] E. Ahedo, S. Correyero, J. Navarro-Cavallé, M. Merino (2020). Macroscopic and parametric study of a kinetic plasma expansion in a paraxial magnetic nozzle. Plasma Sources Science and Technology, 29(4), 045017. https://doi.org/10.1088/1361-6595/ab7855

[24] M. Li, M. Merino, E. Ahedo, H. Tang (2019). On electron boundary conditions in PIC plasma thruster plume simulations. Plasma Sources Science and Technology, 28(3), 034004. https://doi.org/10.1088/1361-6595/ab0949

[25] Á. Sánchez-Villar, J. Zhou, E. Ahedo, M. Merino (2021). Coupled plasma transport and electromagnetic wave simulation of an ECR thruster. Plasma Sources Science and Technology, 30(4), 045005. https://doi.org/10.1088/1361-6595/abde20

[26] N. Souhair, M. Magarotto, E. Majorana, F. Ponti, D. Pavarin (2021). Development of a lumping methodology for the analysis of the excited states in plasma discharges operated with argon, neon, krypton and xenon. Physics of Plasmas, 28(9). https://doi.org/10.1063/5.0057494

[27] L. Brieda, M. Keidar (2012). Development of the Starfish Plasma Simulation Code and Update on Multiscale Modeling of Hall Thrusters. 48th AIAA Joint Propulsion Conference, Atlanta, GA, AIAA-2012-4015. https://doi.org/10.2514/6.2012-4015

[28] J. F. Roussel, et al. (2008). SPIS open-source code: Methods, capabilities, achievements, and prospects. IEEE transactions on plasma science, 36(5), 2360-2368. https://doi.org/10.1109/TPS.2008.2002327

[29] P. Chabert, J. Arancibia Monreal, J. Bredin, L. Popelier, A. Aanesland (2012). Global model of a gridded-ion thruster powered by a radiofrequency inductive coil. Physics of Plasmas, 19(7), 073512. https://doi.org/10.1063/1.4737114

[30] M. A. Lieberman, A. J. Lichtenberg (2005). Principles of plasma discharges and materials processing. John Wiley & Sons. https://doi.org/10.1002/0471724254

[31] F. F. Chen (2012). Introduction to plasma physics. Springer Science & Business Media.

[32] N. Souhair, M. Magarotto, M. Manante, D. Pavarin, F. Ponti (2021). Improvement of a numerical tool for the simulation of a Helicon plasma thruster. Space propulsion 2020+1, On line conference, SP2020-00070.

[33] G. Gallina, M. Magarotto, M. Manente, D. Pavarin (2019). Enhanced biDimensional pIc: an electrostatic/magnetostatic particle-in-cell code for plasma based systems. Journal of Plasma Physics, 85(2), 905850205. https://doi.org/10.1017/S0022377819000205

[34] H. Qin, S. Zhang, J. Xiao, J. Liu, Y. Sun, W. M. Tang (2013). Why is Boris algorithm so good?. Physics of Plasmas, 20(8), 084503. https://doi.org/10.1063/1.4818428

[35] S. Di Fede, M. Magarotto, S. Andrews, D. Pavarin (2021). Simulation of the plume of a Magnetically Enhanced Plasma Thruster with SPIS. Journal of Plasma Physics. https://doi.org/10.1017/S0022377821001057

[36] D. J. Griffiths (2005). Introduction to electrodynamics. https://doi.org/10.1016/B978-1-85573-953-6.50026-X

[37] M. Martinez-Sanchez, J. Navarro-Cavallé, E. Ahedo (2015). Electron cooling and finite potential drop in a magnetized plasma expansion. Physics of Plasmas, 22(5), 053501. https://doi.org/10.1063/1.4919627

[38] F. Trezzolani, M. Magarotto, M. Manente, D. Pavarin (2018). Development of a counterbalanced pendulum thrust stand for electric propulsion. Measurement, 122, 494-501. https://doi.org/10.1016/j.measurement.2018.02.011

[39] F. Romano, et al. (2020). RF helicon-based inductive plasma thruster (IPT) design for an atmosphere-breathing electric propulsion system (ABEP). Acta Astronautica, 176, 476-483. https://doi.org/10.1016/j.actaastro.2020.07.008

[40] A. R. Ellingboe, R. W. Boswell (1996). Capacitive, inductive and helicon-wave modes of operation of a helicon plasma source. Physics of Plasmas, 3(7), 2797-2804. https://doi.org/10.1063/1.871713

[41] A. E. Vinci, S. Mazouffre (2021). Direct experimental comparison of krypton and xenon discharge properties in the magnetic nozzle of a helicon plasma source. Physics of Plasmas, 28(3), 033504. https://doi.org/10.1063/5.0037117

[42] P. Molmud (1960). Expansion of a rarefied gas cloud into a vacuum. The Physics of fluids, 3(3), 362-366. https://doi.org/10.1063/1.1706042

[43] G. Mansutti, et al. (2020). Modeling and design of a plasma-based transmit-array with beam scanning capabilities. Results in Physics, 16, 102923. https://doi.org/10.1016/j.rinp.2019.102923

[44] A. Daykin-Iliopoulos, et al. (2020). Characterisation of a thermionic plasma source apparatus for high-density gaseous plasma antenna applications. Plasma Sources Science and Technology, 29(11), 115002. https://doi.org/10.1088/1361-6595/abb21a

[45] M. Magarotto, P. De Carlo, G. Mansutti, F. J. Bosi, N. E. Buris, A. D. Capobianco, D. Pavarin (2020). Numerical suite for gaseous plasma antennas Simulation. IEEE Transactions on Plasma Science, 49(1), 285-297. https://doi.org/10.1109/TPS.2020.3040008

[46] P. De Carlo, M. Magarotto, G. Mansutti, A. Selmo, A. D. Capobianco, D. Pavarin (2021). Feasibility study of a novel class of plasma antennas for SatCom navigation systems. Acta Astronautica, 178, 846-853. https://doi.org/10.1016/j.actaastro.2020.10.015

[47] P. De Carlo, M. Magarotto, G. Mansutti, S. Boscolo, A. D. Capobianco, D. Pavarin (2021). Experimental Characterization of a Plasma Dipole in the UHF band. IEEE Antennas and Wireless Propagation Letters. https://doi.org/10.1109/LAWP.2021.3091739

[48] M. Saleem (2020). Comparative performance assessment of plasma reactors for the treatment of PFOA; reactor design, kinetics, mineralization and energy yield. Chemical Engineering Journal, 382, 123031. https://doi.org/10.1016/j.cej.2019.123031